

SIMPLE RHEOLOGICAL MODELS OF EUROPEAN TIDEWATER GLACIERS FROM SATELLITE INTERFEROMETRY AND ALTIMETRY

Aleksey I. Sharov⁽¹⁾ and Sven Etzold⁽¹⁾

⁽¹⁾ *Institute of Digital Image Processing, Joanneum Research, Wastiangasse 6, 8010 Graz, Austria*

ABSTRACT

The theory of elastic deformation and the energy conservation principle were applied to simplified rheological modelling of large European tidewater glaciers using the interferometric and altimetric data obtained from the European ERS and American ICESat satellites. Several questions concerning the co-registration, joint interpretation and physical formulation of specific rheological features detected in INSAR interferograms and altimetric transects were analysed and briefly discussed. Transferential approach to analysing fast ice deformations and measuring frontal glacier velocities from *single* SAR interferograms was enhanced. The resultant rheological model allowed frontal velocities and thickness of large glaciers in the Franz Josef Land and Novaya Zemlya archipelagos to be determined and verified thus contributing to the integral estimation of present glacier regime in the European High Arctic.

1. INTRODUCTION

Repeat-pass synthetic aperture radar interferometry (INSAR) offers a hypersensitive instrument for monitoring glacier dynamics, surveying short-term ice velocities and their long-term variations, measuring ice flux and studying mass imbalance of prominent ice sheets and relatively small valley glaciers [1, 2]. Rheological interpretation of INSAR records, which convolve intricately the information on glacier motion, topography and surficial changes, is not always obvious, however, and geometric processing of glacier interferograms is by no means straightforward. The knotty problem of distinguishing between the impacts of ice surface topography and surface displacement on the interferometric phase is conventionally solved by means of differential interferometry (DINSAR) requiring the use of several location-coincident interferograms and necessitating additional reference data, both topographic and rheological.

In classical 2-pass DINSAR approach, the removal of topographic component and manifestation of the motion phase is based on differencing between the original (real) SAR interferogram of a glacier containing both topographic and motion phases and the reference interferogram without motion fringes, which is synthesized from available elevation model (DEM) of the same glacier. Rapid elevation changes and insufficient quality of available DEMs – a problem frequently encountered in glacier studies – is the principal limitation to such approach [3].

Alternatively, in 3- or 4-pass DINSAR approach, two real interferograms can be differenced to cancel the topographic phase and to extract the *differential motion term* under the assumption that glacier topography remains unchanged between INSAR surveys. In order to derive the *absolute motion* from the single differential interferogram one must assume that either the glacier

velocity or the relation between ice-velocity gradients remains constant over the time span covered by both interferograms. Although applicable to rheological modelling in the accumulation area of large ice domes, the assumptions of steady topography and stationary motion have often proved to be incorrect in fast moving and rapidly evolving glacial areas [4].

Furthermore, differential interferometric processing of SAR imagery is exceptionally intolerant of any imperfections in data acquisition and processing, and becomes frequently impossible because of rough topography, rapid changes, incoherent motion, and significant phase noise at glacier margins [5]. Apart from the acquisition of comparable INSAR pairs, which is not an easy matter at the first place, the algorithmic complexity, computational load and processing errors, mostly at the stage of interferometric phase unwrapping, detecting and resolving the line-of-sight motion, and geocoding, bring about further obstacles disappointing those who like to get rapid access to results.

Some time ago, we started experiments related with the direct determination of glacier dynamic quantities from interferometric phase gradients that does not involve complex process artifices and does not require additional topographic reference models [6]. The present paper reports on the continuation of our studies devoted to the simplified rheological and morphological modelling of large European maritime glaciers and assessing glaciomarine interactions along European ice coasts in *single* ERS-1/2 SAR interferograms. Geometric processing and rheological interpretation of 20-look INSAR data has been supported with the additional spaceborne single-pass altimetry data obtained from the ICESAT-GLAS sensor. The major emphasis is put on

- interferometric analysis of the fast-ice deformation and interpretation of glaciomarine interactions along European ice coasts,

- measuring horizontal velocities, strain rate and calving ice flux at fronts of large tidewater glaciers,
- determining the position of ice divides and identifying main drainage basins on the largest European ice caps,
- interferometric modelling of glacier rheology and integral estimation of glacial changes in the Barents Sea region.

This research is considered as a preparatory stage for the upcoming SIGMA and INTEGRAL glaciological projects associated with the launch and operation of the ESA CryoSat mission.

2. EUROPEAN TIDEWATER GLACIERS AND ICE COASTS

Are there tidewater glaciers and ice coasts¹ in Europe? One should answer positively this question. Although there are no glaciers entering the sea at present on the European continent, they are widely distributed in the European arctic archipelagos of Franz Josef Land, Svalbard and Novaya Zemlya, and persist at Jan Mayen Island (Fig. 1, a). Seaward margins of tidewater glaciers form precipitous ice cliffs and walls rising 2 to 50 m and sometimes even 100 m above sea level (Fig. 1, b). The present total length of ice coastlines in the European Arctic can be approximately estimated at 3620 km (Table 1), which accounts for nearly 10 % of the European coastline².

Franz Josef Land (FJL), the northernmost part of the European arctic terra firma, hosts the largest cluster of tidewater glaciers including 245 ice caps³ with slow moving or stagnant seaward margins, and 488 fast moving outlet glaciers draining ice from ice caps into the sea and producing icebergs. Ice shelves are seldom, but not improbable [9]. In the FJL archipelago, 55 from ca. 190 islands are occupied by glaciers and the glacierized coastline extends for ca. 2520 km. The fronts of active outlet glaciers constitute approx. 59 % of the ice coast and contemporary topographic maps and hydrographic charts show more than half of the calving ice coasts by dashed lines, i.e. as uncertain coastlines. Maximum frontal velocities of tidewater glaciers reach 250 (Impetuous Glacier) and even 400 m/a (Karo Glacier). There is some evidence supporting a hypothesis about the presence of surging glaciers (Eastern, Impetuous et al.) in the FJL archipelago.

The total areal extent of glaciation in FJL exceeds 13,500 km² and the mean ice thickness appears to be

¹ Ice coasts are formed by glaciers extending into the sea.

² The coastline of European continent (without islands) stretches for ca. 38,000 km [7].

³ The total number of ice caps in FJL is 347; 102 of them have no maritime margins [8].

close to 180 m. The Southern Glacial Complex covering ca. 2,150 km² on Prince George Land is regarded as the largest ice mass in the archipelago. Renown Glacier is the largest outlet glacier in FJL occupying ca. 380 km² on Wilczek Land.

In the Svalbard archipelago, the number of glaciers entering the sea (10 ice caps and 201 outlet glaciers) is smaller and the total length of ice coasts is shorter (Table 1), albeit the total glacial area (35,100 km², with Kvitøya Island) and the overall mean ice thickness (220 m) are somewhat larger than in FJL. Our recent cartometric estimations showed that the total length of ice coasts in Svalbard was reduced by 14 % in the past 50 years [10]. Typical velocities of 50 - 80 m/a at fronts of Svalbard's tidewater glaciers are relatively low. Most tidewater glaciers in the Svalbard archipelago are of surging type, however, and demonstrate periodically a short-term increase in ice flow velocities up to several meters per day. Frontal velocities of ice flow in Austfonna achieved, for example, 140 m/a [11].

Austfonna Ice Dome (8,120 km²) in north-east Svalbard is the most prominent ice cap in the archipelago with the mean ice thickness of ca. 300 m. In the 1980-s, the total length of its seaward margins was 251 km. This is the 3d largest European glacier after Main Ice Sheet in Novaya Zemlya and Vatnajökull (8,500 km²) in Iceland. Note that there are no tidewater glaciers in Iceland.

Main Ice Sheet (23,778 km²) at North Island of Novaya Zemlya (NZ) is the largest glacier in Europe and the 3d largest mass of ice in the world. Due to the immense size and significant ice thickness reaching 700 m it is frequently referred to as Small Antarctica. There are only 41 outlet glaciers draining ice from the Main Ice Sheet and reaching the sea⁴, and the total length of ice coasts does not exceed 200 km (Table 1). Terrestrial photograph showing glacier front of Shokal'skogo Glacier, typical tidewater glacier in north Novaya Zemlya with a total area of 280 km², and its inferred longitudinal profile are given in Figs. 1 b) and c) respectively. The area of Nordenskjöld Outlet Glacier, the largest in NZ is given as 517.4 km² [12].

Table 1. Length (km) of European ice coasts in the 1950s and 2000s

Period / Region	Franz Josef Land *	Svalbard**	Novaya Zemlya	Jan Mayen Island
1950-s	2661	1050.7	208.4	3.5
2000-s	2522 (- 5%)	903 (-14%)	192 (- 9%)	3.1 (-11%)

*) including Victoria Island; **) including Kvitøya Island

⁴ 27 outlet glaciers reach the Barents Sea and 14 glaciers terminate in the Kara Sea.

Maximum velocity values at fronts of tidewater glaciers vary from glacier to glacier in the range from 50 to 210 m/a, which is somewhat slower than in FJL. Brounova and Petersen glaciers are supposed to be of surging type. The existence in NZ of, at least, partially or transiently floating glacier tongues undergoing tidal movements has been reported in [13].

Several relatively small tidewater glaciers can be found on Jan Mayen Island (Norway). The total area of glaciation on Jan Mayen makes up 120 km² and maximum glacier velocities attain 120 m/a. According to our estimations using available topographic maps and spaceborne imagery, the length of ice coasts at this island has decreased from 3.5 to 3.1 km (-11 %) during the past 50 years. It is worth noting that during the same period of observations the length of ice coasts in the Asian Arctic (Severnaya Zemlya, Ushakova and De Long islands) reduced only for 2 % [10].

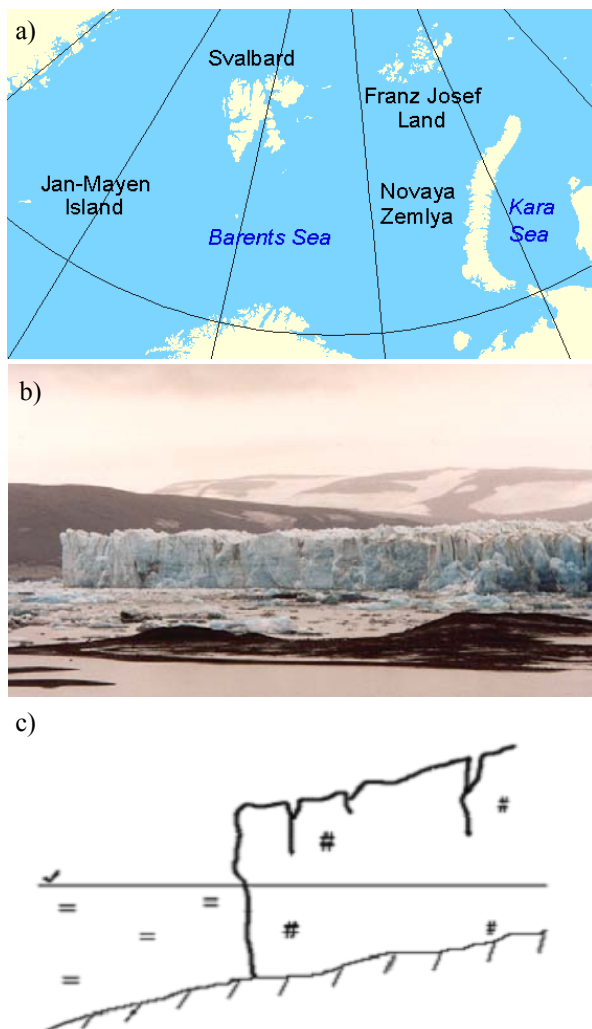


Fig. 1. Locations of European tidewater glaciers (a); terrestrial photograph of Shokal'skogo Tidewater Glacier, NZ (b) and its inferred longitudinal profile (c)

3. DATA GAPS

It is obvious that the European ice coasts standing at the forefront of glaciomarine interactions represent the most varied elements of the arctic coastline, which grow shorter under current environmental settings. The most retreat of ice coasts amounting to several hundred meters across the shore each year was detected at fronts of calving tidewater glaciers. This retreat is presumably related with the dominance of ice-loss processes at glacier fronts including sublimation, melting, marine abrasion and calving over the influx of glacier ice to calving faces. The rate of retreat dL/dt can be defined as a negative difference between the mean ice speed at the glacier front u and the rate of frontal ablation u_c , i.e.

$$dL/dt = u - u_c, \quad (1)$$

where L is the glacier length, t is time interval, and u_c is sometimes called a mean calving speed because the effect of both melting and sublimation is small compared with that of calving of icebergs [14].

Mass-balance estimates are available only for few glaciers, and we still do not know whether the increased ablation mainly effects the current retreat of most European tidewater glaciers or the decelerated ice flow has a guiding influence on their retreat. Hence, both variables in the right part of the Eq.1 are considered as principal unknowns in environmental forcing related to climatic changes.

Calving speed increases with water depth, temperature and longitudinal strain rate, and the ice-coast sensitivity to a change in one or more of these factors depends primarily on the position of the glacier face with respect to the sea level, the ice thickness and the configuration of the glacier bed. The information about the heights of ice coasts given in available topographic maps and hydrographic charts is extremely scarce, obsolete and inaccurate. In the close vicinity of calving ice shores, bathymetric marks are not available, bathymetric contours are broken within 1 km offshore and the possible water depths at ice walls and fronts are usually unknown. Hence, only few data on ice thickness at glacier fronts can be derived from available maps.

There is very little factual knowledge on ice flow velocities at glacier fronts, and the rate of change in ice flow is practically unidentified. The total ice discharge through maritime glacier fronts on a continental scale remains largely uncertain.

The detailed and equivalent rheological models that reliably describe the distribution and variations of frontal glacier velocities and stresses are thus essential for better understanding the evolution of ice coasts, monitoring glaciomarine interactions and adequate

forecasting of possible alterations in the glacier extent. Available 2- or 3-D *numerical* models of glacier flow involving complex equations and numerous variables such as ice temperature, thickness, deformation, bottom melting, etc. are perplexed, cumbersome and error-prone, especially, if applied in the glacier environment different from original applications. The polar idea of the present study is to utilize the simplest *image* models derived from spaceborne INSAR data, which relate the quantities observed in interferometric products with real rheological unknowns on a pixel-by-pixel basis at both local and regional scales.

Ice divides separating adjacent drainage basins on large ice masses set up the spatial limits and boundary conditions for the rheological image modelling of individual outlet glaciers. As soon as the individual drainage basin is identified, one can determine simple glacier morphometric quantities such as length, area, highest positions, etc., and predefine ice flow directions. The most comprehensive morphometric knowledge is collected about the glaciation in Svalbard. The glacier distribution of Svalbard is characterized by distinct asymmetry and the total area of outlet glaciers flowing toward the sea is twice larger than that of glaciers flowing inland [15]. General morphometric characteristics of glaciation in FJL and NZ derived from aerial surveys in the 1950-s [8, 12] are not very reliable at present. Some recent morphometric studies related with the identification of major divides and drainage basins in FJL using spaceborne image data were published in [16]. The exact location of other ice divides still remains uncertain. At the moment of writing this paper we had no reliable data on temporal changes in the structure and location of ice-divides systems on large ice masses in the Barents Sea region. In the view of drastic variations in glacial borders, any evidence for the structural instability in glacial morphology might lead to a number of interesting hypotheses [17].

4. ICE COASTS AND ICE DIVIDES IN SPACEBORNE SAR INTERFEROGRAMS

The representation of ice coasts and ice divides in high-quality INSAR products is mainly determined by

- the type of INSAR product (amplitude, coherence, fringe or phase gradient image),
- INSAR spatial and temporal baseline,
- glacier topography, surface state and motion,
- effects of temporal and geometric decorrelation.

The proper selection of interferometric pairs allows the effects of temporal and geometric decorrelation to be kept small [18]. All 24 ERS-1/2 interferometric pairs used in our study were obtained in October – March 1994-1996 under steady and cold weather conditions with suitable spatial baselines of 0 - 200 m and temporal

intervals of 1 or 3 days between SAR data takes. The INSAR products generated from this data set are free of unfavourable effects due to high winds, heavy clouds, precipitation and melting at the glacier surface.

In our interferograms, all time-stable areas are reproduced with a typical mean coherence value of 0.6 – 0.7, and the interpretation of coherence images, which represent the coefficient of complex correlation between subsequent SAR scenes in shades of grey (Fig. 2, a), does not bring about essential difficulties. Fig. 2 shows, for example, 20-look interferometric pictures of the northern margin of Tindall Ice Dome on Wilczek Land, FJL with several large outlet glaciers flowing into Austrian Channel (South and North Karo glaciers) and Vanderbilt Straight (Milky, Basin 2, and Impetuous glaciers). Glacierized and ice-free coastlines even of small islets, e.g. Gage Island (GI) in Vanderbilt Straight, are well detectable and inland borders of outlet glaciers can be reliably delineated. The lowest mean coherence value of about 0.47 was observed in frontal areas of very fast moving glaciers like South Karo Glacier, the leftmost in Figs. 2, a - d.

A thin dark line separating areas of high coherence on the fast ice and inland can be frequently observed in winter coherence images along coastlines, both precipitous and low-lying. At active glacier fronts, the line becomes interrupted and blurred or even vanishes. At steady coasts, its width usually does not exceed several pixels and we suppose that this effect might be explained by the influence of layover and shadowing in SAR imagery. The line looks similarly to crevasses in sea-ice floes and its interpretation as a coastal fissure in the fast ice, at least locally, may not be excluded.

Highly accelerated ice motion, excessive strain rates and rough surface with numerous crevasses lead to rapid changes in backscattering properties near the glacier face, and the fringe image of glacier exteriors is characterized by low contrast, high local fringe rates and significant phase noise / aliasing (Fig. 2, b, d). Frequently, the direct interferometric analysis of such areas becomes impossible even in tandem INSAR pairs taken in winter [13].

In contrast to calving faces, where the horizontal velocity of ice and the surface roughness attain frequently their maximum, at a symmetric divide on a horizontal bed, the shear stress and horizontal velocity of ice are zero, but the longitudinal stress is high, particularly in the upper layers [19]. Sometimes, major ice divides on large ice caps can be detected as bright stripes with darker surroundings in amplitude and coherence images taken in late winter (May - June) or late summer (late August – early October) [16, 17]. The width of these stripes varies from 150 m to 1000 meters depending on surface topography, and their origin might

be related with melting and refreezing processes, which mostly take place along ice divides because of the low sun elevation. In winter, INSAR products are characterised with homogeneously higher backscattering and coherence values at glacial tops, and the recognition of ice divides becomes more difficult.

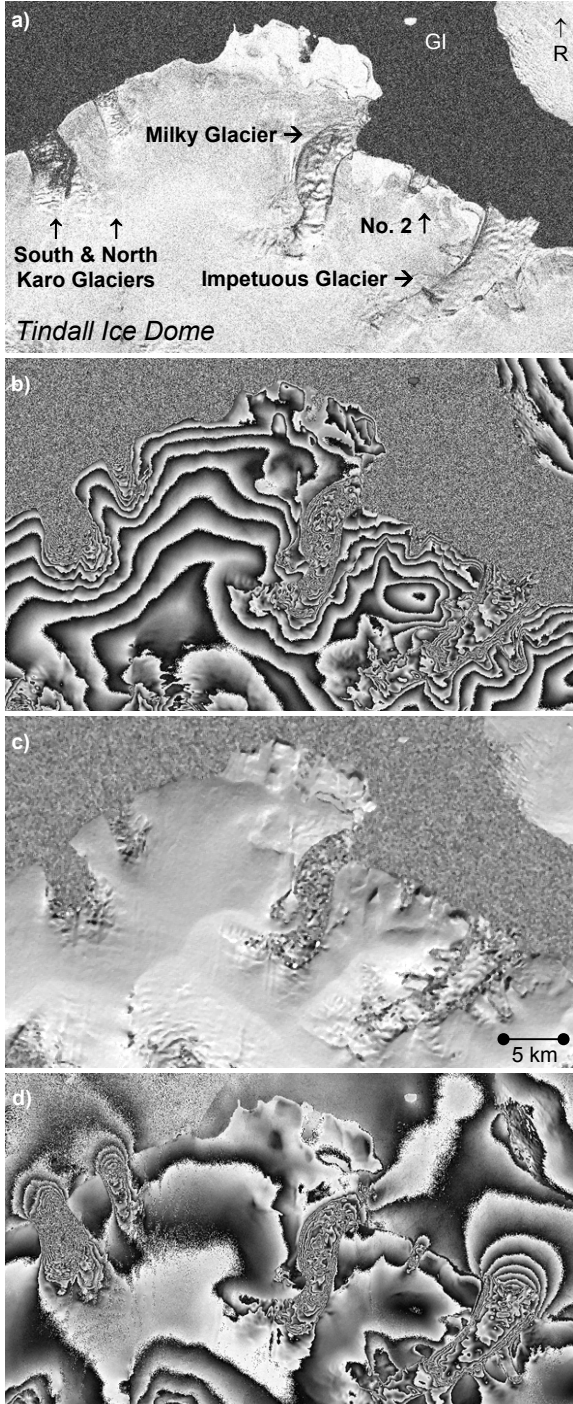


Fig. 2. 20-look INSAR products of Wilczek Land, FJL: coherence image (a), fringe image ($B_n = 129$ m, b) and phase gradient image (c) of 09/10.10.95, fringe image of 17/18.12.95 ($B_n = -43$ m, d)

At best, the identification of ice divides and drainage basins can be performed in a phase gradient image or *topogram*, which is calculated from the original fringe image $\varphi(x, y)$ by using the method of finite (central) differences as [20]

$$\frac{\partial\varphi(x, y)}{\partial x} \cong \frac{\varphi(x + \Delta x, y) - \varphi(x - \Delta x, y)}{2\Delta x} \quad \text{and}$$

$$\frac{\partial\varphi(x, y)}{\partial y} \cong \frac{\varphi(x, y + \Delta y) - \varphi(x, y - \Delta y)}{2\Delta y}. \quad (2)$$

On traversing the divide, the value of the phase gradient clearly changes from negative to positive values. The shift values Δx (in range) and Δy (in azimuth) are equal 1 pixel usually, but, in general, can be manipulated separately in azimuth and range direction within the interval from 0 to several pixels. The increase in the shift value enhances the contrast of elongate crests on ice caps, but amplifies the phase noise and coarsens the spatial resolution of the topogram. The use of SAR interferograms with longer spatial baselines should be preferred in this concern.

Typical topogram showing a complicated system of ice divides in the northern part of Tindall Ice Cap is given in Fig. 2, c. Since each original interferogram of a living glacier contains both topographic and motion phases, the resultant topogram reproduces the glacier surface topography together with the motion component. This is why the ice divides identified in the topogram are referred to as *ice-flow divides*.

5. INSAR REPRESENTATION OF THE FAST SEA ICE ATTACHED TO GLACIER FRONTS

The area of consolidated fast sea ice covering straights of arctic archipelagos for most of the year is often reproduced with quite good coherence and demonstrates good visibility of interferential fringes. Apart from tidal effects, the fast coast ice attached to any active glacier front undergoes the powerful action caused by the glacier motion.

In winter fringe images, the fast-ice displacement / deformation forced by the glacier flow manifests itself as a zone of concentric hemi-elliptical fringes converging at the tips of the glacier front. Such interferential features called “outflows” are permanently found at fronts of *nearly all* tidewater outlet glaciers oriented along the SAR cross-track direction (R); the latter is marked with an arrow in all figures. Outflows have been detected at both open ice shores and in glacial fjords, but we did not observe these features at glacier-free coasts. The lateral extent of outflows may reach 10 kilometers and more. Often albeit not always, the local

coherence within outflows is somewhat lower and the phase noise is higher than outside (Fig. 2, d). This fact might be related with the deformation and lower thickness of sea ice in the area of outflows.

It is believed that the thickness of fast-ice floes and their resistance to stress can influence the shape and the extent of outflow, but not the total number of interferometric fringes within it. Fig. 2, d) shows, for example, the larger extent and the lower rate of motion fringes at the front of Impetuous Glacier, flowing into Vanderbilt Straight with typical ice thickness of 80 to 100 cm, than those at Karo Glaciers terminating in Austrian Channel with commonly thinner (40 - 50 cm) ice [21]. The rate of fast ice displacement / deformation decreases with the distance from the glacier front and increases in the vicinity of natural obstacles such as shoals, other islands, etc. The amount of fast ice displacement usually increases from zero at the tips of the glacier front to its maximum in the mid point at the glacier snout (Fig.2, c).

Fig. 3, a) represents the outflow with somewhat distorted shape located at the front of Shokal'skogo Tidewater Glacier. For the sake of reference Fig. 3, b) provides an amplitude image reproducing the rough surface of glacier front by light tones while the homogeneous area of nearly stationary fast ice nearby appears dark. Note the absence of interferometric fringes on the fast ice surface along the glacier-free coastline to the north and to the south-west from the glacier front.

The general origin of outflows is believed to be related primarily to the *horizontal* displacement of the coastal ice forced by glacial flow because of

- 1) prevailing orientation of outflows along the SAR cross-track direction and the inverse interferometric contrast in outflows observed at outlet glaciers flowing in opposite directions, i.e. toward or away from the sensor;
- 2) enlarged lateral extension of outflows and the increased number of interferential fringes within on SAR interferograms with longer temporal baselines;
- 3) consequent character of outflows in multitemporal interferograms and similarity of phase-gradient patterns over flat glacier margins and outflows;
- 4) no evidence for specific geophysical effects, e.g. tides, currents glacial winds, icings etc., that might control the occurrence and outline of outflows;
- 5) available analogies in the area of interferometric control and fringe projection, c.f. [22].

It is quite clear that vast plane floes of young coastal ice with a very small elevation above sea level (10 – 30 cm) represent an ideal surface for the interferometric analysis of small horizontal motions close to ice coasts and their driving forces. There is no need for

topographic reference in this case ⁵, and the length of spatial baseline becomes a less critical issue. This factor makes it possible to accurately measure frontal glacier velocities in *single* SAR interferograms.

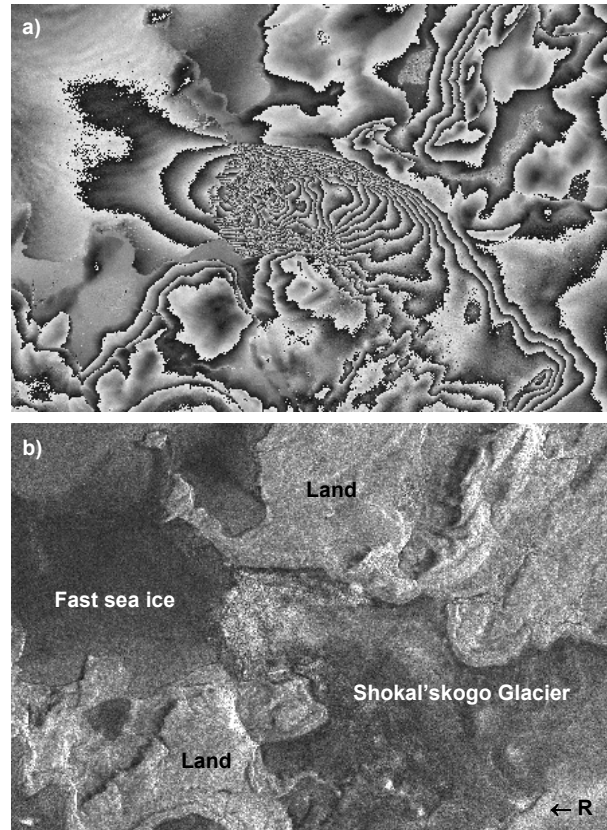


Fig. 3. Fringe image (a) and amplitude image (b) of the SAR interferogram taken on 5/6.03.96 over north NZ

6. MEASUREMENT OF FRONTAL GLACIER VELOCITIES IN SIGLE INTERFEROGRAMS

It is reasonable to assume that in the immediate proximity of the glacier face and under calm weather conditions, the local speed of the fast ice translation is equal to the frontal velocity of gently sloping tongues of tidewater glaciers. Then, in tide-coordinated SAR interferograms without significant tidal effects, the frontal glacier velocity u can be directly determined by counting the number k of interferometric fringes within the corresponding outflow as

$$u \cong 0.5\lambda \cdot k \cdot (T \cdot \cos \beta \cdot \sin \theta)^{-1}, \quad (3)$$

where $\lambda = 5.66$ cm is the wavelength of the SAR signal, β is the flow direction angle measured from the cross-track direction, θ is the viewing angle, and T is the temporal baseline of the interferogram (1 or 3 days).

⁵ Still, there is a necessity for the compensation of tidal effects.

Transverse variations of the frontal velocity along the glacier face can be evaluated by analysing the shape of outflows.

The regular character and rather moderate (50 – 100 cm) heights of semi-diurnal tides in the Barents Sea region allows the magnitude of tidal effects at the instants of SAR surveys to be preliminary estimated by analysing additional tide-gauge data or, at least, data on the moon phase. In fringe images, the influence of tidal effects can be post-estimated through examining the fast-sea-ice motion along glacier-free coasts.

Practical application of this approach known as transferential (from Latin *transferre*: *trans* - across, change + *ferre* to carry) to ERS-1/2-INSAR data processing allowed the frontal velocities of 57 large European tidewater glaciers oriented in the SAR-range direction to be determined for the first time in the history of their remote sensing studies [10]. The frontal velocities of some outlet glaciers were measured several times using different interferograms and the results were very consistent. The velocity values obtained for several study glaciers in FJL and NZ are given in Table 2.

In 20-look tandem interferograms, one cannot reliably recognise outflows at glacial fronts with frontal velocities smaller than 3 cm/day. The maximum measurable velocity depends on several factors (glacier front geometry, sea-ice resistance, temporal baseline) and has yet to be determined. Nevertheless, it is worth noting that we could not measure the frontal velocity of rapidly flowing South Karo Glacier in 3-day interferogram of 23/25.02.1996 because of diffuse edges of fringes and aliasing effects. Note that the velocities given in table 2 are the minimum daily velocities because they were computed using the maximum possible duration (24 hours) of the fast ice deformation.

Table 2. Frontal velocities of tidewater glaciers in FJL and NZ (cold seasons, 1994 – 1996)

Glacier Name	INSAR velocity, cm/day	Date*
<i>Franz Josef Land</i>		
Eastern	18.1	17/18.12.95
Impetuous	27.8 – 45.1	23/25.02.94 - 17/18.12.95
Renown	27.9 – 31.4	23/25.02.94 - 18/19.10.95
Sonklar	30.2	17/18.12.95
South Karo	85.0 – 76.5	17/18.12.95 - 22/23.03.96
<i>North Novaya Zemlya</i>		
Anuchina	7.4 - 10.0 - 7.1	05/06-18/19- 21/22.03.96
Brounova	20.4 - 20.1 - 28.4	05/06-18/19- 21/22.03.96
Inostrantseva	25.4 - 24.4 - 25.9	05/06-18/19- 21/22.03.96
Pavlova	20.5 - 21.7	18/19.03.96 - 21/22.03.96
Shokal'skogo	31.8	05/06.03.96
Vera	47.8 - 44.4	18/19.03.96 - 21/22.03.96

*) most dates correspond to neap tides (the first or third quarter of the moon).

Independent estimates of ice motion from terrestrial surveys performed on 4 test glaciers in north Novaya Zemlya in September 2001 were used for evaluating the absolute accuracy of measuring glacial velocities from winter interferograms. The short-term frontal velocities surveyed in the field at 22 target points were generally consistent with interferometric velocities, although INSAR values were systematically lower, which was explained by seasonal changes in the glacier flow [13]. Some underestimation of frontal glacial velocities in SAR interferograms might occur because of the aliasing errors caused by rapid deformation of the fast ice nearby the ice coast.

7. GLACIER ALTIMETRY

Valuable additional information on the sea ice freeboard and roughness in the areas of permanent outflows was derived from the ICESat-GLAS L1B & L2 lidar altimetry data taken over the study areas in March, October and November 2003. Preliminary interpretation of multitemporal GLA06 altimetry products showed that the ice surface roughness in outflows was mostly greater than that of surrounding ice floes. Fig. 4 shows several typical fragments from the ICESat GLA06 altimetry products representing the sea ice surface roughness and freeboard versus horizontal location in the outflow orthogonal to the Impetuous Glacier front for 12 March (a, b) and 31 October 2004 (c, d). Both dates correspond to the first quarter of the moon (neap tide). The altimetry data were not corrected for local tidal effects. All transects begin at the ice coast, which is not represented due to scaling problems, and terminate in the middle of Vanderbilt Straight. Several concurrent thermal-infrared images obtained from NOAA and ERS-2 satellites were involved in the interpretation of altimetry products. All ICESat altimetric transects were co-registered to available topographic maps 1:200,000.

The ICESat profile of 31.10.03 in Fig. 4, a) demonstrates the presence of moderate deformation in the young fast-sea-ice cover within the outflow. The sea ice thickness grows through time and the sea-ice deformation features within the outflows become especially noticeable in late winter (Fig. 4, c). Careful analysis of a dozen multitemporal altimetry transects showed that, within outflows, the sea ice surface was usually 0.3 – 0.6 m lower than the mean level outside (Fig. 4, b, d). We suppose that the decreased sea ice thickness in outflows is directly related with the glacial forcing, but still don't understand what that is.

Besides, the lidar altimetry data taken in early winter 2003 were applied to measuring the present heights of ice coasts and ice divides in the NZ test site, as well as to studying glacier elevation changes in the ablation area and their relation to changes in the accumulation area. The comparison of 10 altimetric transects with the

hypsothetic profiles derived from topographic maps corroborated the general retreat of ice coasts and showed that some calving faces became 10 to 40 m higher with respect to the sea level. This can be explained by rapid disintegration of thinner frontal parts of tidewater glaciers with corresponding increase of the subaerial part of glacier face. Typical hypsothetic profiles of Petersen Glacier in north NZ derived from the topographic map and ICESat altimetry data are given in Fig. 5. There is a hypothesis on the surging character of this glacier.

To our surprise, the comparison revealed significant positive height changes in the north of the accumulation area of Main Ice Sheet. At elevations ranging from 300 to 600 m a.s.l., the glacier surface became generally higher for 30 – 60 meters, while it lowered for 20 – 30 m at the elevation range of 100 – 250 m (Fig. 5). This finding might play an important role in forecasting future changes of ice coasts in the region. Still, the limited vertical accuracy of topographic maps (standard error of ± 13 m) as well as the influence of the snow accumulation in the fall 2003 on the determined height changes must be accounted for. The analysis of ATSR image data and ICESAT reflectivity profiles did not reveal the presence of low clouds over study glaciers and their influence on the accuracy of altimetric determinations might be excluded.

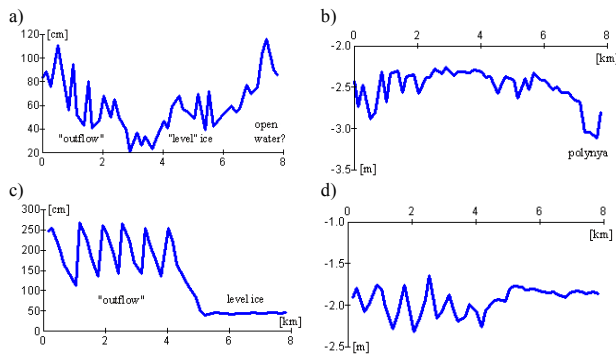


Fig. 4 Sea ice roughness and freeboard close to the Impetuous Glacier Front from ICESat parallel altimetric transects of October 31 (a, b) and March 12, 2004 (c, d).

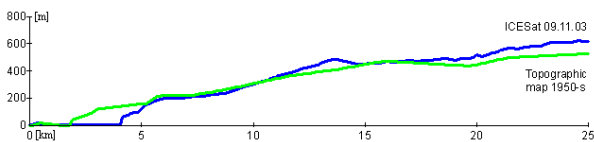


Fig. 5 Hypsothetic profiles AB of Petersen Glacier from topographic map 1:200,000 (1950-s, green) and ICESat altimetry data (09.11.03, blue)

8. JOINT PROCESSING OF INSAR AND ALTIMETRY DATA

Up to now, the terrestrial coverage of study glaciers by the ICESat GLAS data remains rather sparse and altimetric heights can be defined only for some “tie” points on ice coasts and ice divides at widely spaced intervals of several kilometres. In order to define the unknown heights between tie points, we co-registered all available altimetric transects with corresponding interferometric models using the rigorous point-by-point transformation and the ERS-SAR sensor model implemented in the RSG 4.1 software. The co-registration accuracy is characterized with the r.m.s. error of ± 1.2 pixel. Afterwards, the relative height differences between the target and tie points Δh were determined simply by counting the number of interferometric fringes K enclosed between those points with its subsequent multiplication on the value of height ambiguity $h_{2\pi}$ as

$$\Delta h = K \cdot h_{2\pi} \cong 0.5K \cdot \lambda \cdot H \cdot B_n^{-1} \cdot \tan \theta, \quad (4)$$

where $H \cong 785$ km is the height of the satellite above the reference body and B_n is the normal component of the interferometric spatial baseline.

In the case of active ice coasts, some additional correction is needed to compensate the influence of glacier flow on the height measurement. This can be done, e.g. by subtracting the number k of interferometric fringes within the corresponding outflow from the real value K . Apart from measuring glacier heights, which are needed for rheological modelling, such an approach mitigates some local problems related with the procedure of interferometric phase unwrapping at ice cliffs and provides high accuracy of geocoding and change detection at glacier fronts.

An original INSAR composite image of the northern part of Main Ice Sheet consisting of an amplitude image (inland) and fringe image (offshore) with several altimetric transects overlaid is given in Fig.6, a. Digits 1 through 5 denote Inostrantseva, Pavlova, Vera, Bunge and Petersen glaciers respectively. Straight boundary separating the fast sea ice from drift ice is well detectable in the left upper corner. Fig. 6, b represents one of ICESat altimetric transects (blue) across the Main Ice Divide (CD in Fig. 6, a) together with the phase profile (green) from corresponding fringe image. There are no pronounced summits on the altimetric transect near major ice divide, and the divide region appears very flat and broad; its width exceeds 6 km. By contrast, there is a distinct maximum on the phase profile, and, in fringe image, the ice divide area is relatively narrow. We suggest that this could be a result of non-zero surface velocity components, which become

noticeable at distances of only 1-2 kilometres from the ice crest. Given 7-year time difference between the data sets, the local phase maximum in the interferometric profile coincides well (within 500 m) with the highest position (564.1 m) in the divide area on the altimetric transect, c.f. [23]. The effect of radar penetration on the location of ice divides in INSAR products has yet to be studied.

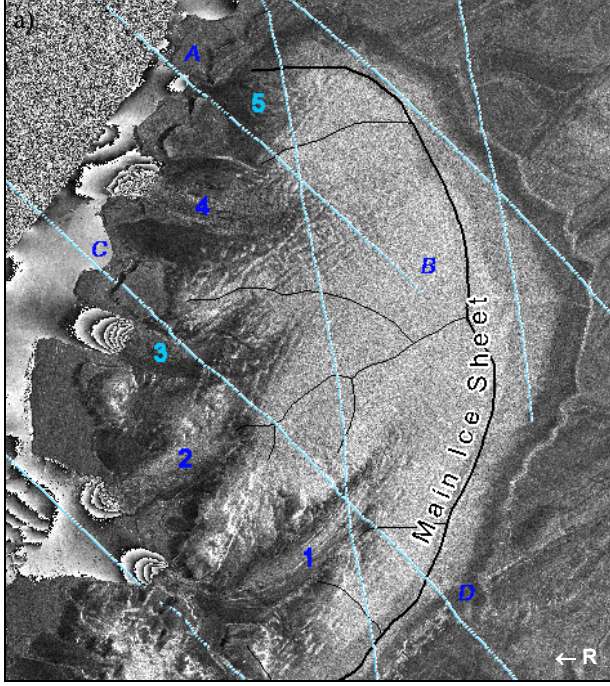


Fig. 6. INSAR composite showing active ice coasts and major ice divides of Main Ice Sheet in north NZ with altimetric transects (cyan) overlaid (a); altimetric and phase profiles CD across the Main Ice Divide (b).

9. FURTHER RHEOLOGICAL INFERENCES

Joint analysis of spaceborne interferograms and altimetry data provides a solid foundation for further rheological inferences and modelling glacier mechanics. A very simple rheological model of glaciomarine interactions along active ice coasts was generated using the theory of elastic deformation and the energy conservation principle. The combined effect of glacial flow, offshore glacial winds and currents, and sea-ice level tilt on the stress state of the fast sea ice can be defined as a superposition of horizontally acting forces

$$-\sigma_i = \sigma_x + \tau_a + \tau_w + \sigma_t, \quad (5)$$

where the acceleration and coriolis terms have been neglected.

Tangential stresses applied to the fast ice due to glacial offshore winds and currents can be determined respectively as

$$\tau_a = \eta \cdot u_a^2 \quad \text{and} \quad \tau_w = \chi \cdot u_w^2, \quad (6)$$

where u_a and u_w are the horizontal velocities of offshore winds and currents at the sea level. Following [24], we took $\eta \cong 2 \cdot 10^{-3} \text{ kg/m}^3$ and $\chi \cong 4.4 \text{ kg/m}^3$ for the practical estimation of wind and water stresses.

Even under strong winds of 10-15 m/s and high roughness of the ice surface the drag of the wind τ_a won't exceed 0.5 Pa. Fast tidal currents of 1.0 m/s occur only in narrow straights of the archipelagos and, in protected glacial bays, the water stress is usually much lower than 0.5 Pa.

The fast-ice stress caused by the surface tilt is given as

$$\sigma_t = -\rho_i \cdot g \cdot z_i \cdot \sin \xi. \quad (7)$$

In Eq. 8, z_i and ρ_i denote the sea ice thickness and density, ξ is the surface slope, and the negative sign implies the ice surface tilt toward the coast. Under average sea ice thickness of 1 m and typical ξ value of 0.005° , the ice-surface-tilt term does not exceed 0.8 Pa.

Transient, random and incoherent effect of these three factors on the deformation of coastal ice is disregarded in our model. The dominant influence on the fast-ice deformation within outflows is believed to be related with the unbalanced horizontal stress at the glacier face caused by permanent glacial flow. Ignoring minor effects of the resistive strain, the depth-averaged value of this driving stress can be estimated from the next basic formula [25]

$$\overline{\sigma_x} \cong 0.5 \cdot \rho_g \cdot g \cdot z_g \cdot \left(1 - \rho_w \cdot \rho_g^{-1} \cdot z_w^2 \cdot z_g^{-2}\right), \quad (8)$$

where $\rho_g = 917 \text{ kgm}^{-3}$ and $\rho_w = 1027 \text{ kgm}^{-3}$ are densities of the glacier ice and sea water respectively; z_g and z_w stand for the glacier ice thickness and the water depth at the terminus, and g is gravitational acceleration.

Typical values of the average ice thickness in frontal parts of our study tidewater glaciers, e.g. those in north NZ, vary from 55 to 120 m, the conjectural water depth

at glacial faces ranges from 30 to 80 m [13], and the estimated minimum value of driving stress $\overline{\sigma_x}$ (in Middle Glacier) exceeds 160 kPa. Shokal'skogo Glacier has a marginal driving stress of ca. 250 kPa.

In the case of elastic uniaxial deformation, the resultant compression of sea ice ε_x is linearly proportional to the stress σ_i , i.e.

$$\sigma_i = E_i \cdot \varepsilon_x = E_i \cdot \frac{\Delta l}{l}, \quad (9)$$

where $E_i \approx 8 \cdot 10^9$ Pa is Young's modulus of ice [26], Δl is the absolute deformation determined by the number k of interferometric fringes enclosed within the corresponding outflow, and l is assumed to be equal to the extent of outflow.

Assuming that the slab of fast ice is tightly frozen to the glacier face and neglecting minor terms in Eq. (5) we obtain

$$-\sigma_i \cong \sigma_x \quad \text{or} \\ -E_i \cdot \frac{\Delta l}{l} \cong 0.5 \cdot \rho_g \cdot g \cdot z_g \cdot \left(1 - \rho_w \cdot \rho_g^{-1} \cdot z_w^2 \cdot z_g^{-2}\right). \quad (10)$$

Despite its symbolical expressivity, Eq. (10) is of low practical use because of ca. 10% uncertainty in the value of parameter E_i . This is why we decided to convert it by supposing that the kinematic energy of a moving terminus is wholly used to surmount the sea ice resistance to deformation, i.e.

$$0.5 \cdot m_b \cdot u^2 = F_i \cdot \Delta l, \quad (11)$$

where $m_b \cong z_g \cdot \rho_g \cdot W_g \cdot b_x$ is the mass of moving glacier block, b_x is the block extension, $F_i = \sigma_i \cdot z_i \cdot W_i$ is the compression strength of sea ice, z_i is the sea-ice thickness and $W_g = W_i$ is the width of glacier face.

Under the supposition of spatially decelerated and temporally instantaneous ($\Delta t = 1$ sec) character of the deformation Δl , the combination of Eqs.10 & 11 yields

$$b_x \cdot u^2 = z_i \cdot g \cdot |\Delta l| \cdot \left(1 - \rho_w \cdot \rho_g^{-1} \cdot q^2\right), \quad (12)$$

where $q = z_w / z_g$, $z_g = z_0 (1 - q)^{-1}$, $z_w = z_0 q (1 - q)^{-1}$ and z_0 is the height of glacier face above the sea level.

Eq. 12 can be solved with regard to q or z_g , if variables u , z_i , z_0 and b_x are known. There were no concurrent interferometric, altimetric and radio-echo sounding data at our disposal, and we had to use the z_i , z_0 and u values obtained in different years, but similar seasons, from

remote sensing surveys and field campaigns as well as the literary and cartographic information on z_g . The variable b_x was used as tuning parameter.

Finally, the glacier thickness at the terminus, an important parameter for the quantitative analysis of frontal ablation and ice discharge through glacier fronts was calculated for several large outlet tidewater glaciers in Wilczek Land, FJL and in north Novaya Zemlya. The thickness values thus obtained correlated well with those reported in [13, 27]. Some relevant values are given in Table 3.

Table 3. Frontal heights of tidewater glaciers in FJL and NZ

Glacier Name	z_0 , m	z_i , m	b_x , m	z_g , m	
				model	field
Middle	25*	1.1	100	63	53*
Petersen	37**	1.3	60	83	80**
Rykachova	59*	1.1	30	86	94*
Shokal'skogo	48*	1.2	20	134	123*
Vera	24*	3.0	30	80	84*
Impetuous	31*	1.7	20	135	125**
Renown	30**	1.6	20	130	138**
South Karo	25**	1.4	10	63	69**

*) state 2000-s, **) state 1950-s

10. CONCLUSIONS

Our numerical experiments coupled with remote sensing observations provided, at least symbolically, a new insight in the mechanics of glaciomarine interactions along active ice coasts and indicated that the character of ice flow at glacier termini might be seriously influenced even by relatively small changes in the sea level and thickness of the fast sea ice attached. To best our knowledge this was the first attempt to quantitatively analyze and model the dynamic interactions between tidewater glacier termini and the fast ice attached to the glacier face from remote sensing data. The study revealed some principal limitations to modern remote sensing methods in measuring small deformations in the fast sea ice. Still, our rheological models involve several simplifying and even intuitive assumptions whose adequacy has to be verified in the field. Also the question about the appropriate temporal scale of rheological modeling remained open, and the detailed study of strain rates in outflow areas using spaceborne phase-gradient images as it was offered in [28] might be very expedient in this concern. Anxiously, we are looking for new concurrent remote sensing data e.g. that to be obtained by ICESat-GLAS and CryoSat-SIRAL altimeters, which could help to answer several open questions and to validate conjectural hypotheses.

ACKNOWLEDGEMENTS

The ERS-1/2-INSAR and ICESat-GLAS data for our studies were generously provided by ESA and NSIDC respectively. The kind assistance of Drs. H.Raggam and L.W.Kenyi from the Joanneum Research in co-registering interferometric and altimetric data is warmly acknowledged.

REFERENCES

1. Goldstein R., Engelhard R., Kamb B., and Frolich R. Satellite radar interferometry for monitoring ice sheet motion: application to an Antarctic ice stream. *Science*, **262**, 1525-1530, 1993.
2. Joughin I., et al. Ice flow of Humboldt, Petermann and Ryder Gletscher, northern Greenland. *J.Glac.*, 45 (150): 231-241, 1999.
3. Gray A.L., et al. Velocities and flux of the Filchner Ice Shelf and its tributaries determined from speckle tracking interferometry. *Can. JRS.*, 27 (3), 193-206, 2001.
4. Nagler T., Mayer C., Rott H. Feasibility of DINSAR for mapping complex motion fields of Alpine ice- and rock-glaciers. Proc. 3d Int. Symp. "Retrieval of Bio- and Geophysical Parameters from SAR Data", 377-382, 2002.
5. Forster R., et al. Interferometric radar observations of Glaciers Europe and Penguin. *J.Glac.*, 45 (150), 325-336, 1999.
6. Sharov A., et al. Methodical alternatives to the glacier motion measurement from differential SAR interferometry. *IAPRS*, XXXIV, 3A: 324-329, 2002.
7. *Geographic Encyclopaedic Dictionary*, Soviet Encyclopaedia, Moscow, 432 p, 1988 (in Russian).
8. Vinogradov O. and Psaryova T. *Catalogue of Glaciers in the USSR: Franz Josef Land*, Hydrometeoizdat, Moscow, 137 p, 1965 (in Russ.)
9. Dowdeswell JA, et al. Evidence for floating ice shelves in Franz Josef Land, Russian High Arctic. *Arctic and Alpine Research* 26: 86-92, 1994.
10. Sharov A. Studying changes of ice coasts in the European Arctic. In: V. Rachold (Ed.) *Arctic Coastal Dynamics. GeoMarine Letters*, 2004 (in press).
11. Dowdeswell J.A., et al. Velocity structure, flow instability and mass flux on a large Arctic ice cap from satellite radar interferometry. *EPSL*, 167, 131-140, 1999.
12. Varnakova G.M. and Koryakin V.S. *Catalogue of Glaciers in the USSR: Novaya Zemlya*. Hydrometeoizdat, Leningrad, 112 p, 1978 (in Russ.)
13. Sharov A., Glazovskiy A., and Meyer F. Survey of glacial dynamics in Novaya Zemlya using satellite radar interferometry. *Zeitschrift für Gletscherkunde und Glazialgeologie*, 38, 1-19, 2003.
14. Hanson B. and Hooke R.L. Glacier calving: a numerical model of forces in the calving-speed/water-depth relation. *J.Glac.* 46, 188-196, 2000.
15. Troitsky L.S., et al. *Glaciation of Svalbard*. Nauka, Moscow, 276 p, 1975 (in Russ.)
16. Dowdeswell J.A., et al. Ice divides and drainage basins on the ice caps of Franz Josef Land, Russian High Arctic, defined from Landsat, KFA-1000, and ERS-1 SAR satellite. *Arctic and Alpine Research*, 27 (3), 264-270, 1999.
17. Sharov A. *Digital photogrammetric mapping in the European High Arctic using spaceborne imagery*. Unpublished PhD thesis, TU Graz, 143 p, 1997.
18. Sharov, A. and Gutjahr K. Some methodological enhancements to INSAR surveying of polar ice caps. Proc. 21st EARSeL Symp., 65-72, 2002.
19. Paterson W.S.B. *The physics of glaciers*. 3d edition, Pergamon Press, Oxford, 1994.
20. Sharov A. Gradient approach to INSAR modelling of glacial dynamics and morphology. Proc. 22^d EARSeL Symp., Millpress, Rotterdam, 373-381, 2003.
21. Matishov G.G. (Ed.) *Environment and ecosystems of the Franz Josef Land archipelago and shelf*. Apatity, 262 p., 1993
22. Muramatsu M., et al. The projection diagram. *Applied optics*, 42 (23), 4765-4771, 2003.
23. Zwally H.J. and Li Jun. Seasonal and interannual variations of firm densification and ice sheet surface elevation at the Greenland summit. *J.Glac.*, 48 (161): 231-241, 2002.
24. Dammert P., Leppäranta M. and Askne J. Sea ice displacement measured by ERS-1 SAR interferometry. Proc. 3rd ERS Symp., Florence, 1997, <http://earth.esa.int/workshops/ers97/papers/dammert/092c.htm>.
25. Van der Veen C.J. Tidewater calving. *J.Glac.*, 42 (141), 375-385, 1996.
26. Hooke R. *Principles of glacier mechanics*. Prentice Hall, New Jersey, 1998.
27. Vil'chinskii A.V., et al. Ice flow modelling on outlet glaciers of Wilczek Land, Franz Josef Land. *Data of Glaciological Studies*, 85, 178-186, 1998 (in Russ.)
28. Sharov A. and Etzold S. Full-value mapping of glacier rheology using repeat pass SAR interferograms. Proc. Fringe'03 workshop. ESA, ESRIN, Frascati, 2003 (in press).